# Twisted bilayer graphene as a linear nanoactuator

Zhisen Meng,[1] Zhenyan Wu,[1] Jesús Carrete,[2] and Zhao Wang[1,*]
[1]*Guangxi Key Laboratory for Relativistic Astrophysics, Department of Physics, Guangxi University, 530004 Nanning, China*
[2]*Institute of Materials Chemistry, TU Wien, A-1060 Vienna, Austria*

(Received 23 September 2019; revised 1 October 2020; accepted 5 October 2020; published 26 October 2020)

We propose a linear actuation mechanism for twisted bilayer graphene. Using molecular dynamics simulations, we show that the translational motion of a layer can cause another layer to move in an orthogonal direction. Such an effect depends strongly on the crystallographic orientation of graphene with respect to the direction of displacement. For the cross junction between two graphene nanoribbons, we predict the existence of a linear and a nonlinear actuation regime separated by a critical bilayer twisting angle. This critical angle is determined by the overlap between the van der Waals interaction ranges of the moiré superlattice. Based on this mechanism, a linear nanoactuator with desired transmission efficiency can be designed by adjusting the interlayer twisting angle of bilayer graphene.

DOI: 10.1103/PhysRevB.102.155424

## I. INTRODUCTION

Gears are among the oldest inventions of mankind—the earliest example dating from the fourth century BC [1]—but their importance has only grown with time. They are still essential in modern machines and even with a view to future nanotechnology for nanodevices with moving parts. The design of a gear at the nanoscale is particularly challenging, however, due to difficulties in implementing well-positioned gear teeth (presumably small molecules or clusters) on nanostructures [2,3]. Even if one manages to overcome that obstacle, the gear will still suffer from strong friction and adhesion between nanometer-sized components due to their extreme surface-to-volume ratio [4,5]. The lack of an effective motion-transmission system therefore remains a critical problem for the top-down design of nanomachines inspired by their macroscopic counterparts [6].

Graphene has emerged as a promising building block of nanoscale devices owing to its peculiar structure, superior mechanical strength, high thermal conductivity, and chemical stability [7]. For the design of nanoscale gears, bilayer graphene is particularly interesting since it provides a self-assembled junction that could possibly be frictionless in relative movement [8]. These features are given rise by the overlap between the $\pi$ orbitals of graphene layers determined by the specific relative angle between them, known as the bilayer twisting angle, which also leads to other interesting physical phenomena such as superconduction [9]. The adhesion of junctions between the closely related carbon nanotubes has been reported to depend on the overlapping sequence of $\pi$ orbitals [10–15]. These previously reported features have revealed a possibility of using $\pi$-$\pi$ stacking to transmit motion between $sp^2$ carbon nanostructures. However, machines based on nanotubes face practical problems due to the difficulty of controlling the rotational motion of individual one-dimensional nanostructures [16]. Therefore, here we study bilayer graphene as the equivalent of a linear actuator in order to approach an experimentally realizable system. Using molecular dynamics (MD) simulations, we demonstrate that the displacement of a graphene layer can spontaneously cause a neighboring layer to move in a perpendicular direction at room temperature. The transmission efficiency is found to be adjustable by tuning the crystalline orientation of the graphene layers with respect to the sliding direction. A transition from linear to nonlinear motion transmission is predicted for the cross junction between graphene nanoribbons for a relative bilayer twisting angle larger than a critical value.

## II. METHODS

In our MD simulations, a graphene nanoribbon (GNR) is superimposed on top of another to form a cross van der Waals (vdW) junction, as shown in Fig. 1(a). After initial velocities are randomly assigned to the atoms, the layer is brought to thermal equilibrium at 300 K with a Langevin thermostat. The driving layer $L_1$ is then pulled along the $y$ axis at a constant speed of 0.005 Å/ps, while the driven layer $L_2$ can move freely along the $x$ and $z$ directions. The driving layer is fixed as a rigid body in such a process, while the temperature of the driven layer is controlled to be approximately 300 K by the Langevin thermostat with a damping factor of 0.1 ps. The interlayer spacing adjusts spontaneously to the dynamic equilibrium distance. The GNRs are infinite (periodic) in length with hydrogen-saturated edges. The movement of $L_2$ in the $y$ direction is constrained in order to produce gear effects, just like in the macroscopic counterparts of the actuator device. Each simulation runs for 12.0 ns with a time step of 1.0 fs. The simulations are conducted within the MD package LAMMPS [17]. An example input script is provided in the Supplemental Material for the ease of interested readers to reproduce the same simulation [18].

*zw@gxu.edu.cn

 

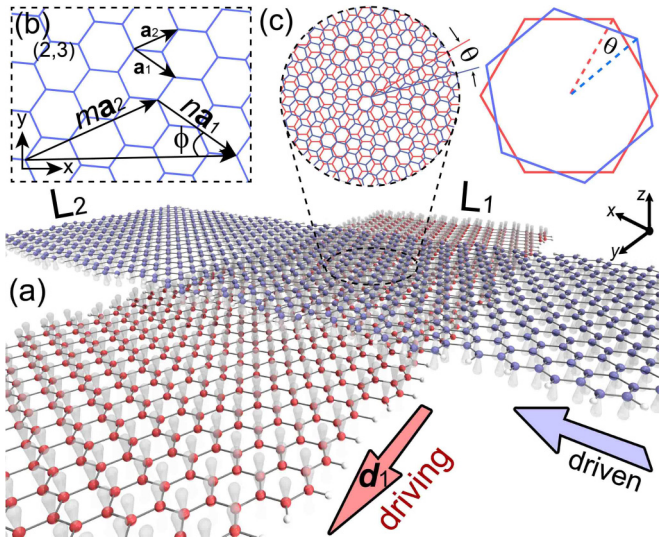


FIG. 1. (a) Model setup for a junction between two GNRs $L_1$ and $L_2$. The red and blue arrows indicate the displacement directions. The cone networks illustrate how electron orbitals are stacked on top of each other. (b) Schematic depiction of the crystallographic angle $\phi$ of graphene. (c) The zoomed-in picture of the moiré pattern shows the definition of the relative bilayer (twisting) angle $\theta$.

The crystallographic orientation of the layer is defined by the relative angle $\phi$ between the zigzag direction in graphene lattice and its longitudinal direction [19], as illustrated in Fig. 1(b). A bilayer angle $\theta$ is generated by twisting a layer at the cross junction to be the relative angle formed by the chiral vectors of the two layers as shown in Fig. 1(c). Twenty-five instances of GNR junctions with different values of $\theta$ were simulated, as listed in Table I.

The total potential energy of the system ($\varepsilon$) consists of the intralayer covalent interactions in $L_1$, the corresponding term for $L_2$, and the noncovalent interlayer interaction between them:

$$\varepsilon = \sum_{i=1}^{N_1-1} \sum_{j=i+1}^{N_1} \varepsilon_{ij}^{\mathrm{cov}} + \sum_{k=1}^{N_2-1} \sum_{l=k+1}^{N_2} \varepsilon_{kl}^{\mathrm{cov}} + \sum_{i=1}^{N_1} \sum_{k=1}^{N_2} \varepsilon_{ik}^{\mathrm{vdW}}, \tag{1}$$

where $i$, $j$ and $k$, $l$ run over the total number of atoms in $L_1$ and $L_2$ ($N_1$ and $N_2$), respectively.

$\varepsilon^{\mathrm{cov}}$ is calculated using the second generation of the reactive empirical bond-order (REBO) force field, in which the total interatomic potential involves many-body terms. The parametrization and benchmarks for this potential have been provided elsewhere [20,21]. Note that the REBO potential has been shown to afford a good description of the structural flexibility of graphene and similar nanomaterials in our previous works [22,23].

The Kolmogorov-Crespi (KC) force field is employed to describe the interlayer interaction potential $\varepsilon^{\mathrm{vdW}}$,

$$\varepsilon_{ik}^{\mathrm{vdW}} = e^{-\lambda(r_{ik}-z_0)}[C + f(\rho_{ik}) + f(\rho_{ki})] - A\left(\frac{r_{ik}}{z_0}\right)^{-6}, \tag{2}$$

where $f$ is a rapidly decaying function of the transverse distance $\rho$,

$$f(\rho) = e^{(-\rho/\delta)^2} \sum_{n=0}^{2} C_{2n}(\rho/\delta)^{2n}, \tag{3}$$

where $\rho_{ik}^2 = r_{ik}^2 - (\boldsymbol{n_i} \cdot \boldsymbol{r_{ik}})^2$ and $\rho_{ki}^2 = r_{ik}^2 - (\boldsymbol{n_k} \cdot \boldsymbol{r_{ik}})^2$, and $\boldsymbol{n_i}$ and $\boldsymbol{n_k}$ are surface normals at atomic sites $i$ and $k$, respectively. We have used the parameter values of this force field provided in Ref. [24] with a cutoff radius of 14 Å. The KC model was proposed to improve the description to the overlapping of the $\pi$ electrons with respect to the classical Lennard-Jones potential, which has been reported to underestimate the surface energy corrugation.

## III. RESULTS AND DISCUSSION

We start by simulating the idealized case of two identical superimposed graphene layers that are infinite in length and width. Different crystallographic orientations with respect to the displacement direction are considered, characterized by the crystallographic angle $\phi$ [Fig. 1(b)]. When $L_1$ is pulled along the $y$ axis by a distance $d_1$, $L_2$ will slide along the $x$ axis in response with an amplitude $d_2$, as illustrated in Fig. 2(a). It is found that $d_2$ is roughly proportional to $d_1$ on large time scales, with a proportionality constant that strongly depends on $\phi$. More specifically, greater values of $\phi$ lead to faster sliding. This effect is similar to the gear motion of concentric carbon nanotubes observed by Barreiro *et al.* using an atomic force microscope [25]. In their experiment, it was found that the translational and the rotational motions of the outer tube strongly depend on the nanotube chirality, which is analogous

TABLE I. List of simulated GNR junctions.

| Sample | $\phi$ (°) | Width (Å) | $\theta$ (°) | Sample | $\phi$ (°) | Width (Å) | $\theta$ (°) | Sample | $\phi$ (°) | Width (Å) | $\theta$ (°) |
|---|---|---|---|---|---|---|---|---|---|---|---|
| 1 | 0.00 | 24.60 | 30.00 | 10 | 28.26 | 40.50 | 26.52 | 18 | 17.99 | 41.38 | 5.98 |
| 2 | 4.70 | 25.92 | 20.57 | 11 | 30.00 | 42.61 | 30.00 | 19 | 20.17 | 43.24 | 10.35 |
| 3 | 8.95 | 27.39 | 12.10 | 12 | 0.00 | 31.98 | 30.00 | 20 | 22.17 | 45.16 | 14.35 |
| 4 | 12.73 | 29.00 | 4.54 | 13 | 3.67 | 33.29 | 22.66 | 21 | 24.01 | 47.13 | 18.01 |
| 5 | 16.10 | 30.73 | 2.20 | 14 | 7.05 | 34.70 | 15.89 | 22 | 25.69 | 49.14 | 21.39 |
| 6 | 19.11 | 32.54 | 8.21 | 15 | 10.16 | 36.24 | 9.68 | 23 | 27.25 | 51.19 | 24.49 |
| 7 | 21.79 | 34.44 | 13.57 | 16 | 13.00 | 37.87 | 3.99 | 24 | 28.68 | 53.27 | 27.35 |
| 8 | 24.18 | 36.40 | 18.36 | 17 | 15.61 | 39.59 | 1.21 | 25 | 30.00 | 55.39 | 30.00 |
| 9 | 26.33 | 38.43 | 22.66 | | | | | | | | |

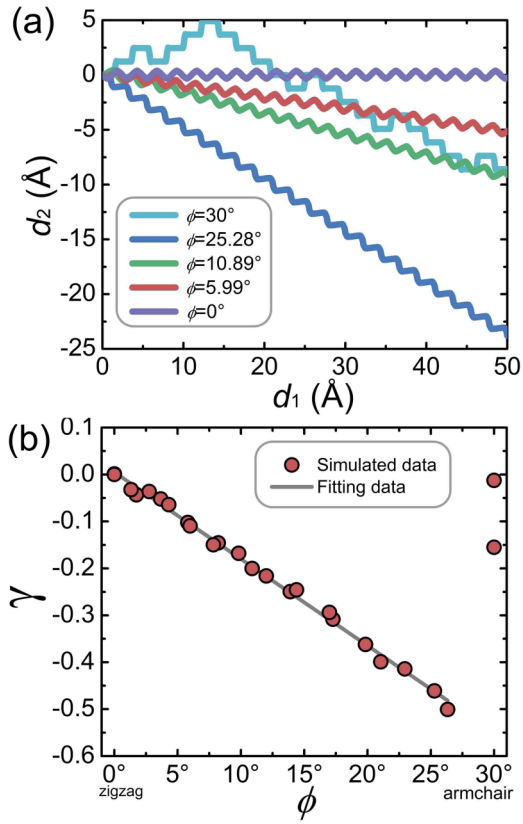


FIG. 2. (a) Displacement of $L_2$ in $x$ vs that of $L_1$ in $y$ for two infinite graphene layers with the same crystallographic angle $\phi_1 = \phi_2 = \phi$ (and therefore a relative bilayer angle $\theta = 0$). (b) Transmission factor $\gamma = \bar{d}_2/\bar{d}_1$ vs $\phi$ for different cases.

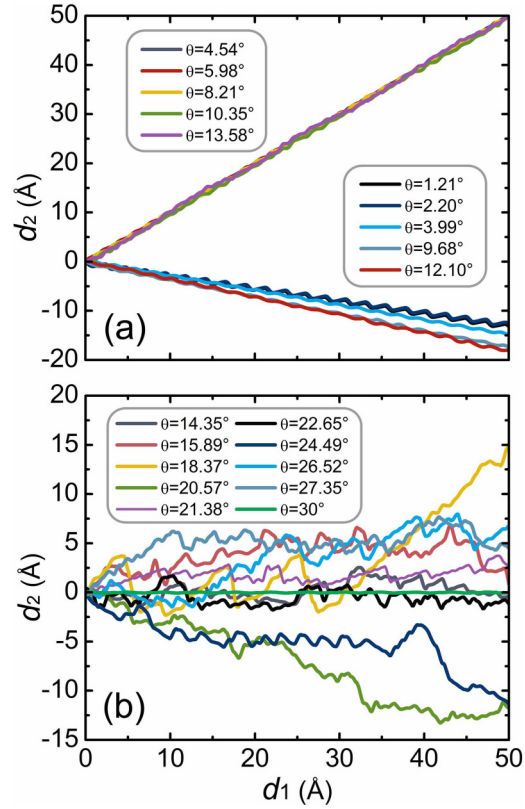


FIG. 3. Displacement of $L_2$ in $x$ vs that of $L_1$ in $y$ for the GNRs listed in Table I, which form cross junctions with different values of the relative crystallographic angle (so-called twisting angle) $\theta$ ranging (a) from 0° to 13.58° or (b) from 14.35° to 30°.

to the crystallographic orientation of graphene considered in this work. The clear exceptions to this trend are the two special cases of $\phi = 0$ and $\pi/6$. In those cases, $L_2$ simply oscillates along $x$, with periods corresponding to the dimensions of a unit cell of the graphene lattice along the zigzag and armchair directions, respectively, 2.46 Å and 4.26 Å [19].

The efficiency of motion transmission of this linear actuator can be represented by a transmission factor,

$$\gamma = \frac{\bar{d}_2}{\bar{d}_1}, \tag{4}$$

which gives the slope of curves like the ones in Fig. 2(a). Figure 2(b) shows the values of $\gamma$ as a function of $\phi$. With the exception of the value for $\phi = \pi/6$, the slope is a well-defined linear function of the crystallographic angle and can be parametrized as $\gamma = -1.018\phi + 0.005$ for $0 \leqslant \phi < \pi/6$, reaching a minimum of $\sim -0.5$ among the measured samples and a value of zero for $\phi = 0$ as expected. The $\phi = \pi/6$ case can also be captured by a periodic extension of this linear function, with a period of $\pi/6$.

We next consider a realistic scenario of a cross junction between two nanoribbons that are infinite (periodic) in length but finite in width, as schematically depicted in Fig. 1(a). Like in the idealized case of infinite bilayer graphene, when $L_1$ is forced to slide along $y$ by an amount $d_1$, $L_2$ spontaneously moves along $x$ by $d_2$, a value strongly dependent on the bilayer twisting angle $\theta$. We find that smaller values of $\theta$ lead to linear actuation as illustrated in Fig. 3(a), while the response of $L_2$ to the movement of $L_1$ is nonlinear for junctions with larger $\theta$ as shown in Fig. 3(b). For the simulated samples with $\theta \leqslant 13.58°$ listed in Table I, $d_2$ is roughly proportional to $d_1$ on large scales, with oscillations with a spatial period corresponding to the length of a cell of graphene [Fig. 3(a)]. It can also be seen that the proportionality constant of these actuators can be either positive or negative for $L_2$ sliding along $x$ or $-x$, respectively.

A more quantitative view into the efficiency of motion transmission in this system is provided by Fig. 4(a), which shows the transmission factor $\gamma$ as a function of the bilayer angle $\theta$. It can be seen that the transmission ratio is divided into two different regions with a threshold at a critical value of $\theta_c \approx 13.58°$. The motion transmission is roughly linear when $0 < \theta < \theta_c$, but the behavior changes dramatically for $\theta_c < \theta \leqslant \pi/6$. To understand the separation of the linear and the nonlinear regions, in Figs. 4(b)–4(e) we plot the distribution of potential energy (DPE) on the graphene surface for four different cross-junction samples (Samples 17, 19, 14, and 23 in Table I).

The carbon atoms in graphene exhibit $sp^2$ hybridization, whereby each of them builds three in-plane $\sigma$ bonds leaving a $\pi$ orbital pointing in the direction normal to the surface. This leads to an "eggbox" potential energy landscape [26–28]. Therefore, there are specific directions along which two stacked graphene layers can slide more easily, just like

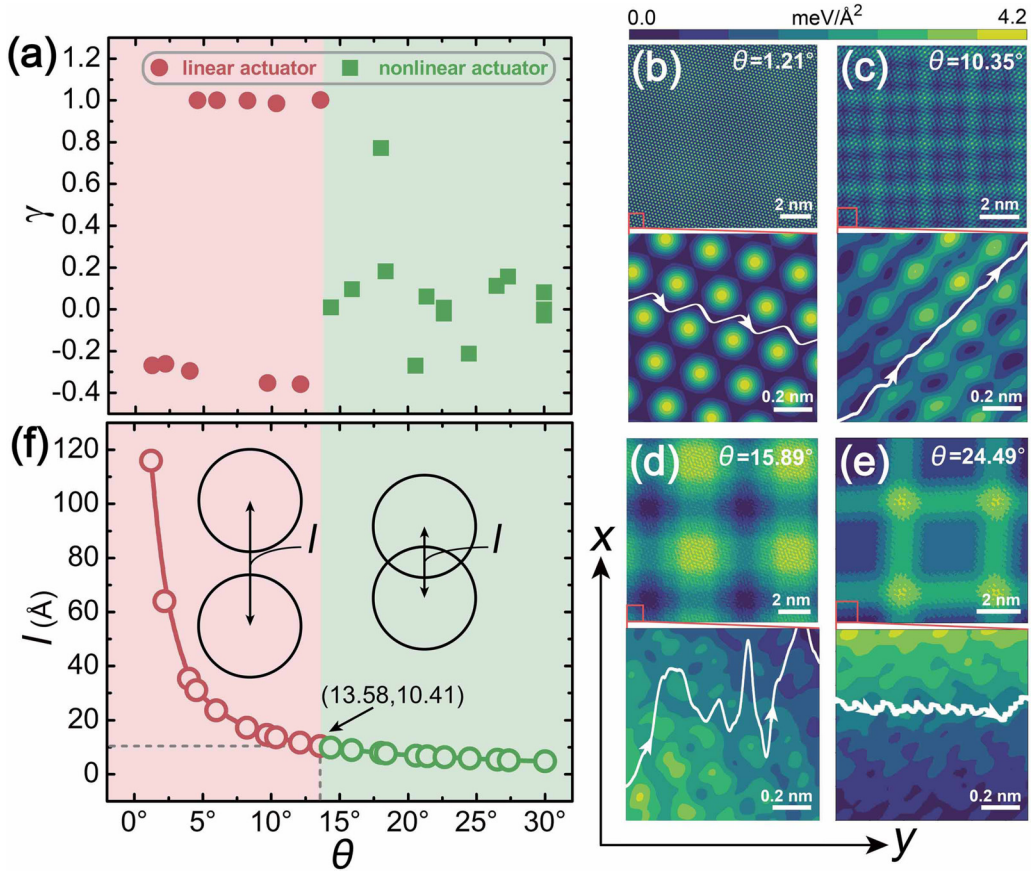


FIG. 4. (a) Transmission factor $\gamma$ vs $\theta$ for the samples listed in Table I. (b–e) Distribution of potential energy for GNR junctions of different bilayer angle $\theta$. The color map represents the interaction energy per unit of surface area of the junction in meV/Å$^2$. The arrows point along minimum-energy paths. (f) Moiré wavelength as a function of $\theta$ according to Eq. (5). The inset shows the overlap of the vdW interaction ranges of the two layers of the moiré superlattice for different ranges of twisting angles.

in the case of two real eggboxes facing each other. When the driving layer $L_1$ is pulled, $L_2$ will tend to follow those minimum-energy paths (MEPs), as illustrated with arrows in the enlarged energy landscapes in the bottom panels of Figs. 4(b)–4(e). The data for the figures were obtained by displacing $L_2$ atop $L_1$ in both longitudinal and transverse directions while keeping a fixed minimum interlayer spacing of 3.35 Å. Figures 4(b) and 4(c) show why $L_2$ will move in a specific direction in response to the movement of $L_1$, i.e., why a change along the horizontal axis (displacement of $L_1$) will lead to a displacement along the vertical axis (movement of $L_2$). In contrast, $d_2$ will not linearly increase with increasing $d_1$ in the case of Figs. 4(d) and 4(e) due to the disordered energy landscape of the sample with $\theta = 15.89°$ and 24.49°.

The disordered energy landscape is a result of the overlap of the periodic vdW interaction ranges of the moiré superlattice, caused by rotational misalignment of the lattice in the cross junctions [29]. Specifically, the response of $L_2$ to the displacement of $L_1$ becomes nonlinear with increasing $\theta$ when the periodic length of a moiré cell $l$ falls below the vdW interaction cutoff, which is typically considered to be 3 times the vdW equilibrium distance ($\approx 3.4$ Å for graphite) [21]. This is to be expected, since $l$ decreases with increasing $\theta$ as

$$l = \frac{a}{2\sin\left(\frac{\theta}{2}\right)}, \tag{5}$$

where $a = 2.46$ Å is the lattice constant of graphene. The critical moiré wavelength corresponding to $\theta_c = 13.58°$ is approximately 10.41 Å as shown in Fig. 4(f). The overlap of the vdW interaction spheres introduces a perturbation to the periodicity of the potential energy landscape by breaking its symmetry and produces perturbed DPEs like those shown in Figs. 4(d) and 4(e), which lead to nonlinear motion transmission.

Another interesting aspect of the linear motion transmission of bilayer graphene is the discrepancy between the positive and the negative transmissions. This can also be understood with the help of the DPE maps. For instance, Fig. 4(b) shows a negative motion transmission at $\theta = 1.21°$, while Fig. 4(c) shows a positive motion transmission at $\theta = 10.35°$. The difference in the motion transmission direction is reflected by the different orientation of the MEP in the energy landscape. It is found that the sign of the the transmission factor is dependent not only on the bilayer twisting angle $\theta$ but also on the crystallographic angle $\phi$, as shown in Fig. 5(a). A small $\theta$ or a small $\phi$ will most likely lead to

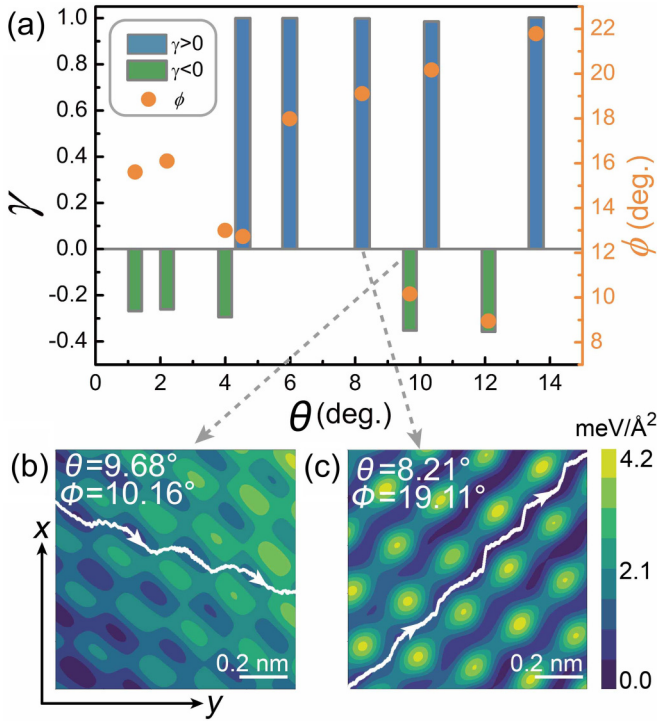


FIG. 5. (a) Left axis (vertical bars): Transmission factor $\gamma$ of the linear actuators among the samples vs bilayer twisting angle $\theta$. Right axis (circles): The corresponding crystallographic angle $\phi$ of these samples. (b) Distribution of potential energy (DPE) on the graphene surface for two samples (Nos. 15 and 6 in Table I). The arrows point along MEPs.

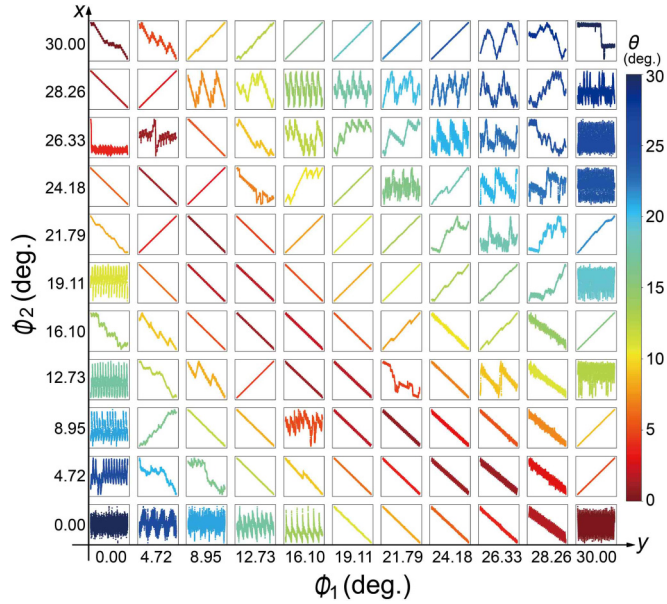


FIG. 6. Displacement of $L_2$ in $x$ vs that of $L_1$ in $y$ for the cross junctions of 121 pairs of GNRs of different crystalline orientations. The scale of the horizontal axis is 60.0 Å in total, while that of the vertical axis is adjusted to fit the same panel dimension. The color scale corresponds to the value of the bilayer twisting angle $\theta$.

negative transmission, whereas most positive motion transmission is observed to be at large values of $\theta$ and $\phi$. The typical parallelogram-shaped landscape of the vdW potential is preserved at small twisting angle $\theta$ as shown in Fig. 4(b), in which the transmission is most likely to be negative since the direction of one of the MEPs (indicated by the white arrow) exhibits a small angle to the direction of $y$. However, the shape of the energy landscape can be significantly modified by a large twisting angle $\theta$ as shown in Figs. 5(b)–5(c). There are two different cases at large $\theta$. One is the situation with a small $\phi$, which leads to a MEP toward $-x$ as shown in Fig. 5(b), while the other corresponds to a large $\phi$, leading to barriers in $-x$ and a minimum-energy path in the positive direction as shown in Fig. 5(c).

We focus on the cross junctions of GNRs with the same crystalline orientation in the aforementioned results. One may wonder if the cross junctions of GNRs with different crystalline orientations will follow the same physical trend. To answer this question, we have extended our simulation to 121 pairs of GNRs of different crystalline angles beyond the combinations listed in Table I. More specifically, we took the first 11 GNR samples listed in Table I and simulated the cross junctions constructed by all the pair combinations of them. The results shown in Fig. 6 reveal that the linear actuation behavior roughly holds for bilayer GNRs with small $\theta$ (the red part), while the response becomes nonlinear in the case of large twisting angle (the blue part). This trend is similar to that was shown within Fig. 4(a). Moreover, a further analysis shows that a few exceptions in Fig. 6 may possibly be correlated with the effect of the ribbons' width on the actuation as shown in the Supplemental Material [18].

## IV. CONCLUSION

A gear mechanism is predicted for bilayer graphene, which is shown to be capable of transmitting motion in orthogonal directions based on interlayer vdW interactions. The transmission ratio depends on the crystallographic orientation of the graphene layers. In the case of cross junctions of GNRs, the motion transmission is found to be strongly dependent upon the bilayer twisting angle $\theta$. Linear actuation is obtained for junctions with small $\theta$, while nonlinear actuation is observed for junctions with bilayer twisting angles larger than a critical threshold of $\theta_c \approx 13.58°$. This threshold is likely to be determined by the overlap between the vdW interaction ranges in the moiré superlattices of bilayer graphene, or by the lack thereof. Our results suggest that linear nanoactuators with desired transmission efficiency can be obtained by adjusting the interlayer angle of layered two-dimensional nanostructures.

## ACKNOWLEDGMENTS

We acknowledge partial financial support from the National Natural Science Foundation of China (Grant No. 11964002), the Guangxi Science Foundation (Grant No. 2018GXNSFAA138179), and the Scientific Research Foundation of Guangxi University (Grant No. XTZ160532).

[1] J. Needham, *Science and Civilisation in China, Volume 4: Physics and Physical Technology, Part 2: Mechanical Engineering* (Cambridge University, Cambridge, England, 1965).
[2] J. Han, A. Globus, R. Jaffe, and G. Deardorff, Nanotechnology **8**, 95 (1997).
[3] G. S. Kottas, L. I. Clarke, D. Horinek, and J. Michl, Chem. Rev. **105**, 1281 (2005).
[4] L. F. Boesel, C. Greiner, E. Arzt, and A. del Campo, Adv. Mater. **22**, 2125 (2010).
[5] W. Guo, Z. Wang, and J. Li, Nano Lett. **15**, 6582 (2015).
[6] S. H. Kim, D. B. Asay, and M. T. Dugger, Nano Today **2**, 22 (2007).
[7] A. H. Castro Neto, F. Guinea, N. M. R. Peres, K. S. Novoselov, and A. K. Geim, Rev. Mod. Phys. **81**, 109 (2009).
[8] J. C. Spear, B. W. Ewers, and J. D. Batteas, Nano Today **10**, 301 (2015).
[9] U. Mogera and G. U. Kulkarni, Carbon **156**, 470 (2020).
[10] Y. B. Chen, Z. Y. Shen, Z. W. Xu, Y. Hu, H. T. Xu, S. Wang, X. L. Guo, Y. F. Zhang, L. M. Peng, F. Ding *et al.*, Nat. Commun. **4**, 2205 (2013).
[11] Z. Wang, Carbon **151**, 130 (2019).
[12] Z. Wang, Phys. Rev. B **100**, 035430 (2019).
[13] M. R. Falvo, J. Steele, R. M. Taylor, and R. Superfine, Phys. Rev. B **62**, R10665 (2000).
[14] R. Guerra, I. Leven, A. Vanossi, O. Hod, and E. Tosatti, Nano Lett. **17**, 5321 (2017).
[15] K. Cai, H. Yin, Q. H. Qin, and Y. Li, Nano Lett. **14**, 2558 (2014).
[16] B. Bourlon, D. C. Glattli, C. Miko, L. Forro, and A. Bachtold, Nano Lett. **4**, 709 (2004).
[17] S. Plimpton, J. Comput. Phys. **117**, 1 (1995).
[18] See Supplemental Material at http://link.aps.org/supplemental/10.1103/PhysRevB.102.155424 for an example LAMMPS input script and results of simulation with various ribbon widths.
[19] M. S. Dresselhaus, G. Dresselhaus, and P. Avouris, *Carbon Nanotubes Synthesis, Structure, Properties, and Applications* (Springer-Verlag, Berlin, 2001).
[20] D. W. Brenner, O. A. Shenderova, J. A. Harrison, S. J. Stuart, B. Ni, and S. B. Sinnott, J. Phys.: Condens. Matter **14**, 783 (2002).
[21] S. J. Stuart, A. B. Tutein, and J. A. Harrison, J. Chem. Phys. **112**, 6472 (2000).
[22] Z. Wang and M. Devel, Phys. Rev. B **83**, 125422 (2011).
[23] H. Qi, S. Picaud, M. Devel, E. Liang, and Z. Wang, Astrophys. J. **867**, 133 (2018).
[24] A. N. Kolmogorov and V. H. Crespi, Phys. Rev. B **71**, 235415 (2005).
[25] A. Barreiro, R. Rurali, E. R. Hernandez, J. Moser, T. Pichler, L. Forro, and A. Bachtold, Science **320** (2008).
[26] Z. Wang, J. Phys. D **52**, 385301 (2019).
[27] Z. Wang, J. Phys. Chem. C **123**, 15166 (2019).
[28] Z. Wang, J. Phys. Chem. C **124**, 3851 (2020).
[29] Z. Y. Rong and P. Kuiper, Phys. Rev. B **48**, 17427 (1993).